Supporting Information for:

Methane transport and sources in an Arctic deep-water cold seep offshore NW Svalbard (Vestnesa Ridge, 79°N)

Simone Sauer[1]*, Wei-Li Hong[2], Haoyi Yao[1], Aivo Lepland[2], Martin Klug[2], Florian Eichinger[3], Tobias Himmler[2], Antoine Crémiere[4], Giuliana Panieri[1], Carsten J. Schubert[5], Jochen Knies[2]

[1]CAGE – Centre for Arctic Gas Hydrate, Environment and Climate, UiT-The Arctic University of Norway, Department of Geosciences, 9037 Tromsø, Norway
[2]Geological Survey of Norway, 7491 Trondheim, Norway
[3]Hydroisotop GmbH, Schweitenkirschen, Germany
[4]Division of Geological and Planetary Sciences, California Institute of Technology, Pasadena, California, USA
[5]EAWAG, Swiss Federal Institute of Aquatic Science and Technology, Kastanienbaum, Switzerland
*current affiliation : IUEM-Institut Universitaire Européen de la Mer, LEMAR, Rue Dumont d'Urville, 29280 Plouzané, France.

Contents

1 Model setup:

1.1 Model environment parameterization for PC017

We consider a 45 cm sediment column for a time span of 20 years. The 20 years are chosen to ensure all processes approach a quasi-steady state. Longer time spans are possible but not necessary as the results, both in pore fluid and sediment phases, will not significantly change after 20 years. Time and depth discretization, dt and dx, are 0.0013 years and 0.0037 meters, respectively. These values were chosen after repeated tests for numerical stability. For best numerical stability, we adopted an implicit numerical scheme for time and space iteration.

1.2 Pore fluid chemical species and solid phase considered

We considered eight solute species and five solid phases. These include ^{12}DIC, ^{13}DIC, $^{12}CH_4$, $^{13}CH_4$, SO_4^{2-}, Ca^{2+}, and NH_4^+ for pore fluid species and ^{12}C-carbonate, ^{13}C-carbonate, ^{12}C-POC, and ^{13}C-POC.

Conservation of sediment volume

The model was constructed by conserving the bulk sediment volume

$$\frac{\partial(M_x^t)}{\partial t} = \frac{\partial F_x^t}{\partial x} + \Sigma R_x^t \qquad (1)$$

M: mole/gram of material in bulk sediments as a function of depth and time

F: volumetric flux of material (mole or gram/m^2 bulk sediment/year)

R: sum of different reactions considered as a function of depth and time (mole or gram/m^3 bulk sediment /year).

t and *x:* time (yr) and depth (m).

For the solutes, the following equation was applied:

$$\frac{\partial(\phi_{f.x}^t S_x^t)}{\partial t} = \frac{\partial(D_x^t \frac{\partial(\phi_{f.x}^t S_x^t)}{\partial x} - (v_{f.x}^t + v_{ext.x}^t)\phi_{f.x}^t S_x^t)}{\partial x} + \Sigma R_{f.x}^t \qquad (2)$$

$\phi_{f.x}^t$: pore fluid volume fraction as a function of depth and time

S_x^t: solute concentrations as a function of depth and time

$v_{f.x}^t$: pore fluid burial velocity as a function of depth and time (m bulk sediment/yr)

$v_{ext.x}^t$: external fluid velocity as a function of depth and time (m bulk sediment/yr)

D_x^t: diffusion coefficients as a function of depth and time (m^2 bulk sediment/yr)

$\Sigma R_{f.x}^t$: sum of reactions for the solute as a function of depth and time (mole /m^3 bulk sediment/yr)

For the different solid phases, the following equation is applied:

$$\frac{\partial[\phi_{s.x}^t C_x^t]}{\partial t} = -\frac{\partial[v_{s.x}^t \phi_{s.x}^t C_x^t]}{\partial x} + \Sigma R_{s.x}^t \qquad (3)$$

$\phi_{s.x}^t$: dry sediment volume fraction as a function of depth and time

C_x^t: weight of the different solid in dry sediments as a function of depth and time

$v_{s.x}^t$: dry sediment burial velocity as a function of depth and time (m bulk sediment/yr)

$\Sigma R_{s.x}^t$: sum of reactions for the solid phase (gram carbonate or organic matter/m^3 bulk sediments/yr)

Porosity, solute diffusion, and advection of sediment package

A constant porosity value was assigned throughout the initial sediment column. Downcore porosity is updated at every iterative calculation to account for the observations that the growth of authigenic minerals likely takes up significant pore space:

$$\phi_{f.x}^t = \phi_{f.x}^{t-1} - \sum \frac{(C_x^t - C_x^{t-1})\phi_{s.x}^{t-1}}{\rho} \qquad (4)$$

ρ: density of the solid phases of interest.

Diffusion coefficients for the eight solutes are also adjusted depending on the porosity values at each iteration:

$$D_x^t = \frac{D_{SW}}{1 - Ln(\phi_{f.x}^{t\,2})} \qquad (5)$$

D_x^t: Diffusion coefficients for the various solutes in the porous media (m^2 bulk sediments/yr).

D_{SW}: diffusion coefficient for the various solutes in seawater at -0.5 ºC (m^2 bulk sediments/yr).

$\phi_{f.x}^t$: porosity as a function of depth and time (m^3 pore space/m^3 bulk sediments)

D_{SW} for the solutes considered are reported in Tab. S1. Advective transport of the sediment package occurs during the burial of sediments. Both sediment particles and pore fluid are buried with different rates ($v_{s.x}^t$ and $v_{f.x}^t$) which results in the relative upward movement of fluid with respect to the sediment particles of the same age. The initial advection terms are formulated following the steady-state compaction assumption (Boudreau, 1997):

$$v_{f.x}^t = \frac{U_f}{\phi_{f.x}^t} = \frac{\phi_{f.inf} v_{inf}}{\phi_{f.x}^t} \quad (6)$$

$$v_{s.x}^t = \frac{U_s}{\phi_{s.x}^t} = \frac{\phi_{s.inf} v_{inf}}{\phi_{s.x}^t} \quad (7)$$

U_f and U_s: volumetric flux of pore fluid/dry sediments

v_{inf}: burial velocity at an infinite depth

We include additional pore fluid advection:

$$v_{ext.x}^t = -p v_{f.x}^t \quad (8)$$

p: a positive scaler

Table S1: Diffusion coefficients in seawater (unit: m^2/yr) at -0.5 °C (Boudreau, 1997)

Pore water constituent	Diffusion coefficient in seawater (Dsw)
^{12}C-DIC and ^{13}C-DIC	1.55×10^{-2}
^{12}C-CH4 and ^{13}C-CH4	2.91×10^{-2}
Ca^{2+}	1.11×10^{-2}
NH_4^+	2.93×10^{-2}
SO_4^{2-}	1.5×10^{-2}

1.3 Biogeochemical reactions

The nine reactions considered are formulated following a generic form:

$$R = k \times \Sigma C \times DC$$

ΣC refers to all the concentrations of solute/solid that determine the magnitude of the rate. *k* includes the kinetic constants as well as the dependency on other solutes which are not directly involved in the reaction of interest. *DC* refer to "dimension correction" which converts the different space dimension (pore space or dry sediment space) to bulk sediment space. It is noted that our rate formulation is semi-empirical (as compared to the more theory-based formulation of reaction rates in other geochemical simulation software (see: Steefel et al., 2015) which provides certain flexibility and also includes important theoretical considerations. All the *R* terms are in the unit of mole/m^3(bulk sediment)/yr. All the kinetic constants, *k*, have an identical unit of yr^{-1} with the ΣC terms having different units for solute or solid species (mole/m^3 (pore space) and wt/m^3 (dry sediment) respectively). It is important to note that our *k* are apparent kinetic constants for the ease of model implementation. This is, however, different from the formulation for enzymatically catalyzed reactions which consider activity for solutes (instead of concentration) and theoretical maximum rates (instead of apparent kinetic constants). We do however include the terms to describe how the microbial reaction rates should vary under low, but non-depleted, substrate level. Also, the inhibition of reactions by specific solute species is also included by assigning *Error functions*.-We consider nine reactions in this model:

Net anaerobic oxidation of methane (AOM) coupled to sulfate reduction (SR) (R_{AOMSR}):

$^{12/13}CH_4 + SO_4^{2-} \rightarrow f^{12/13}HCO_3^- + HS^- + (1\text{-}f)\ ^{12/13}$(ANME biomass)

This represents the net reaction after considering both the forward and backward reaction as described by (Yoshinaga et al., 2014) (i.e., $f^+ - f^-$). While most of the methane carbon is oxidized and transferred the DIC pool (in the form of bicarbonate), a small fraction (1-f) of the methane carbon is assimilated into the ANME biomass. The magnitude of R_{AOMSR} is determined as follows:

$$^{12/13}R_{AOMSR} = {}^{12/13}k_{AOM} \times \frac{[SO_4]}{[SO_4]+K_{half-SO4}} \times \left[{}^{12/13}CH_4\right] \times Erf([CH_4]) \times \phi_{f.x}^t$$

The reaction rate depends on sulfate concentration and will be greatly reduced when the concentration is over 2 mM as controlled by $K_{half-SO4}$ (i.e., Monod-type kinetic expression, $K_{half-SO4} = 2\ mM$). No such term is added to methane as no threshold concentration exists for either $^{12}CH_4$ or $^{13}CH_4$ but only for the total methane concentration (i.e., $^{12}CH_4$+$^{13}CH_4$; (Nauhaus et al., 2002; Vavilin, 2013)). In order to switch off the reaction when methane concentration drops to a certain threshold value, we assigned the error function for such control. The isotopic fractionation of this reaction is described by the ratio between $^{12}k_{AOM}$ and $^{12}k_{AOM}$ (Rees, 1973):

$\alpha_{AOM} = {}^{12}k_{AOM}/{}^{13}k_{AOM} = 1.002$

Back flux reaction of AOM (R_{AOMCR}):

$^{12/13}DIC \rightarrow {}^{12/13}CH_4$

This process is the CO_2 reduction that occurs at the enzyme level which is needed to account for the light isotopic signature around the SMT (Yoshinaga et al., 2014). The rate of the reaction is expressed as:

$$^{12}R_{AOMCR} = \left({}^{12}R_{AOMSR} + {}^{13}R_{AOMSR}\right) \times \frac{r_{AOMCR}}{r_{AOMCR}+1} \times Erf\left(\frac{K_{inhib-SO4}}{[SO_4]}\right)$$

$$^{13}R_{AOMCR} = \left({}^{12}R_{AOMSR} + {}^{13}R_{AOMSR}\right) \times \frac{1}{r_{AOMCR}+1} \times Erf\left(\frac{K_{inhib-SO4}}{[SO_4]}\right)$$

$$r_{AOMBF} = \frac{\alpha_{CR} \times {}^{12}DIC}{{}^{13}DIC}$$

The $Erf\left(\frac{K_{inhib-SO4}}{[SO_4]}\right)$ ($K_{inhib-SO4}$ = 1 mM) term determines the proportion of net AOMSR rate that is back flux reaction (i.e., similar to the f^-/f^{net} in Yoshinaga et al. (2014)) which depends on sulfate concentration. The bulk carbon transferred during the back flux is then partitioned to ^{12}C and ^{13}C according to r_{AOMCR} which takes into account the isotopic fractionation during CO_2 reduction, α_{CR} (=1.1) (Whiticar, 1999).

CO_2 reduction (R_{CR}):

$^{12/13}DIC \rightarrow {}^{12/13}CH_4$

This reaction is different from the AOM back flux in that it is not operated at the enzyme level but utilizes any CO_2 produced regardless of the DIC sources (Hong et al., 2013; Hong et al., 2014; Pohlman et al., 2009). The rate is formulated as follows:

$$^{12/13}R_{CR} = {}^{12/13}k_{CR} \times \left[{}^{12/13}DIC\right] \times Erf\left(\frac{K_{inhib-SO4}}{[SO_4]}\right) \times \phi_{f.x}^t$$

The error function determines when and where this process will occur according to the sulfate concentration. The isotopic fractionation is assigned by:

$\alpha_{CR} = {}^{12}k_{CR}/{}^{13}k_{CR}$

Incorporation of DIC and CH_4 into ANME biomass ($R_{DIC-ASS}$ and $R_{CH4-ASS}$):

$R_{DIC-ASS}$: $^{12/13}DIC + 0.25*NH_4 \rightarrow {}^{12/13}POC$

$R_{CH4-ASS}$: $^{12/13}CH_4\ 0.25*NH_4 \rightarrow {}^{12/13}POC$

Incorporation of DIC and CH_4 is formulated separately in the model.

$$^{12/13}R_{DIC-ASS} = (1-f) \times ({}^{12}R_{AOMSR} + {}^{13}R_{AOMSR}) \times \frac{^{12/13}DIC}{^{12}DIC + {}^{13}DIC} \times \frac{NH_4}{NH_4 + K_{half-NH4}}$$

$$^{12/13}R_{CH4-ASS} = (1-f) \times {}^{12/13}R_{AOMSR} \times \frac{NH_4}{NH_4 + K_{half-NH4}}$$

The difference of these two reactions is that $R_{CH4-ASS}$ inherits directly the isotopic signature from methane as R_{AOMSR} only depends on the concentrations of ^{12}C and ^{13}C methane. $R_{DIC-ASS}$ partitions of total carbon involved according to the isotopic signature of the bulk DIC pool. As NH_4 is incorporated during POC formation, the reaction rate will be greatly diminished when NH_4 concentration is lower than a certain threshold ($K_{half-NH4}$ = 0.01 mM) according to the Monod-type kinetic expression. The stoichiometry for NH_4 is obtained from Nauhaus et al. (2007). No isotopic fraction is assigned.

POC degradation through SR and fermentation (R_{POC-SR} and R_{POC-ME}):

R_{POC-SR}: $^{12/13}POC + 0.5SO_4 \rightarrow {}^{12/13}DIC + N/C\ NH_4$

R_{POC-ME}: $^{12/13}POC \rightarrow {}^{12/13}DIC + N/C\ NH4$

The reaction rates are formulated as:

$$^{12/13}R_{POC-SR} = {}^{12/13}k_{POC-SR} \times \frac{[SO_4]}{[SO_4] + K_{half-SO4}} \times \frac{[^{12/13}POC] \times \phi^t_{s.x}}{MW_{12/13POC}}$$

$$^{12/13}R_{POC-ME} = {}^{12/13}k_{POC-ME} \times \frac{[^{12/13}POC] \times \phi^t_{s.x}}{MW_{12/13TOC}} \times\ Erf(\frac{K_{inhib-SO4}}{[SO_4]})$$

Where MW stands for molecular weight. No isotopic fraction is assigned for both reactions.

Formation of authigenic carbonate (R_{CP}):

$^{12/13}R_{CP}$: $^{12/13}DIC + Ca \leftrightarrow {}^{12/13}Carbonate$

The precipitation and dissolution of these authigenic minerals are determined by the corresponding solubility product K_{sp}:

$K_{sp.calcite}$ = 4.9204E-7 (25 ^oC, 100 bar, 35 psu)

The saturation state of the mineral, Ω, is then defined as:

$\Omega_{calcite} = [Ca^{2+}][CO_3^{2-}]/\ K_{sp.calcite}$

Ω>1: saturated and Ω<1: undersaturated

The concentration of CO_3^{2-} is calculated from the DIC concentration with the knowledge of the acidity constants, K_1 and K_2, for the carbonic acid. Values of 7.6984E-7 and 4.0453E-10 are adopted, respectively, as calculated from Zeebe and Wolf-Gladrow (2001) for -0.5 ºC and 35 PSU.

The rates of precipitation (when Ω>1) are formulated as:

$$^{12/13}R_{CP} = {}^{12/13}k_{CP} \times [{}^{12/13}DIC] \times \frac{[Ca]}{[Ca]+K_{half-Ca}} \times \phi_{f.x}^{t}$$

The Monod term ($K_{half-Ca}$ = 8 mM) for calcium is to account for the general observation that downcore dissolved calcium concentration usually approaches an asymptotic value indicating the absence of carbonate precipitation despite the oversaturation status of pore fluid. The rates of dissolution (when Ω<1) are formulated as:

$$^{12/13}R_{CP} = {}^{12}k_{CP} \times [12calcite] \times Erf([12calcite] + [13calcite]) \times \phi_{s.x}^{t}$$

Precipitation of calcite slows down when the concentrations of pore fluid calcium and sulfate approach the half-saturation constants for dissolved calcium ($K_{half-Ca}$), which was determined based on the fitting with the porewater data.

1.4 Initial and boundary conditions

We adopt seawater composition for the top boundary condition and initial condition of the model. No authigenic calcite was buried from the seafloor with 1 wt% of TOC assigned for the top boundary condition. Initial condition for all solid phases, except TOC, was set to be zero. How to determine the lower boundary condition for all solutes is a complicated issue. A no flux lower boundary condition assumes no material is transported across the lower boundary of the model. In other words, the changes of concentrations in the deepest model cell are only determined by the reactions we assigned and the transport from shallower cells. When specific solute concentrations are assigned as lower boundary conditions, the underlying assumption is that the modeled sediment column is in constant contact with a fluid with fixed composition at all time during the model run. Such assumption is sometimes difficult to justify as we can hardly obtain any information beyond the sediment depth recovered. In our case, such assumption may be reasonable as our sediments are likely influenced by an upward advecting fluid. We chose different lower boundary conditions based on the situations of the sites modeled. See main test for justification of different bottom boundary conditions used.

2 Model test runs for PC017

No external advection of fluid:

The modelled DIC concentrations are highest at the SMT and δ^{13}C-DIC values are lowest at the SMT and increase below the SMT due to CO_2 reduction which consumes DIC and produces CH_4 with a large isotopic fractionation (Figure S1). Although the SMT depth and the δ^{13}C-CH_4 profile match with the data, this model does not match the measured DIC and δ^{13}C-DIC values. Modelled DIC concentrations are way lower than the observed values, as are the δ^{13}C-DIC values around the SMT. Towards the bottom of the core the modelled δ^{13}C-DIC values are higher than the measured ones. Furthermore, the measured Ca^{2+} profile shows a much steeper decrease in the upper 10 cmbsf than the modelled profile.

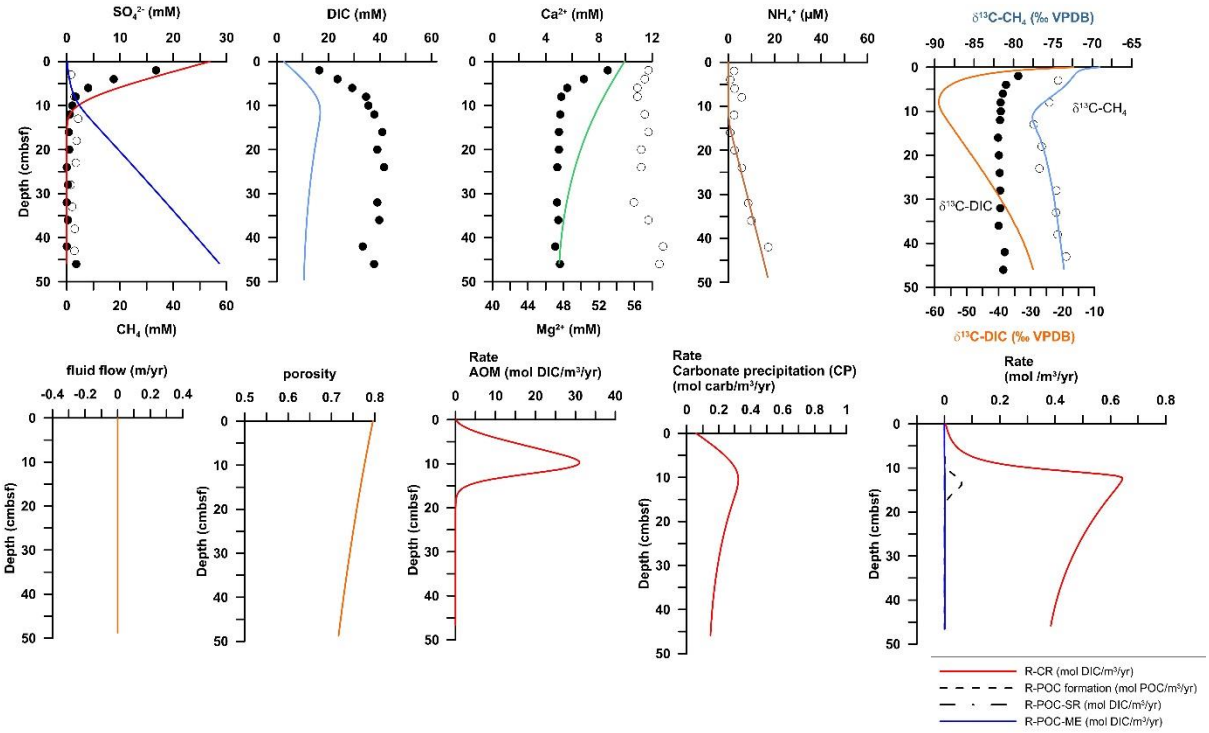

Figure S1: Model results for PC017 with no external fluid advection. The black dots represent measured pore water data, the solid lines represent the best fit of our model. The upper right graph includes measured data for δ^{13}C-DIC (filled dots) and δ^{13}C-CH4 (circles). The lower right graph includes the depth profiles of the rates of CO_2 reduction (R-CR) organoclastic sulphate reduction (R-POC-SR) and organic matter degradation by fermentation (R-POC-ME), and organic matter formation by the AOM microbial consortium (R-POC formation). Rates of AOM, POC-SR, POC-ME and R-CR are all expressed in mol DIC/m^3/yr to make them easier to compare.

No CO_2 reduction and no external fluid advection:

The re-modelled δ^{13}C-DIC profile now has a similar shape as the data but shifted to lower values by around 25‰ (Figure S2). The low δ^{13}C-DIC values modelled below the SMT simply reflect downward diffusion of DIC with low δ^{13}C-DIC values due to the absence of reactions below the SMT which fractionate the carbon isotopes. Again, modelled DIC values are too low, as in the previous run. The maximum modelled DIC concentration can only be ca. 21 mM, as a result of AOM-produced DIC (which is 28 mM, equivalent to sulphate consumption) minus DIC consumption due to carbonate precipitation (ca. 7mM deduced from the Ca^{2+} profile). Also, the modelled δ^{13}C-CH_4 values in this run are slightly too high. The modelled CH_4 concentration in this and the previous run have to be set extremely high to create the observed shallow SMT.

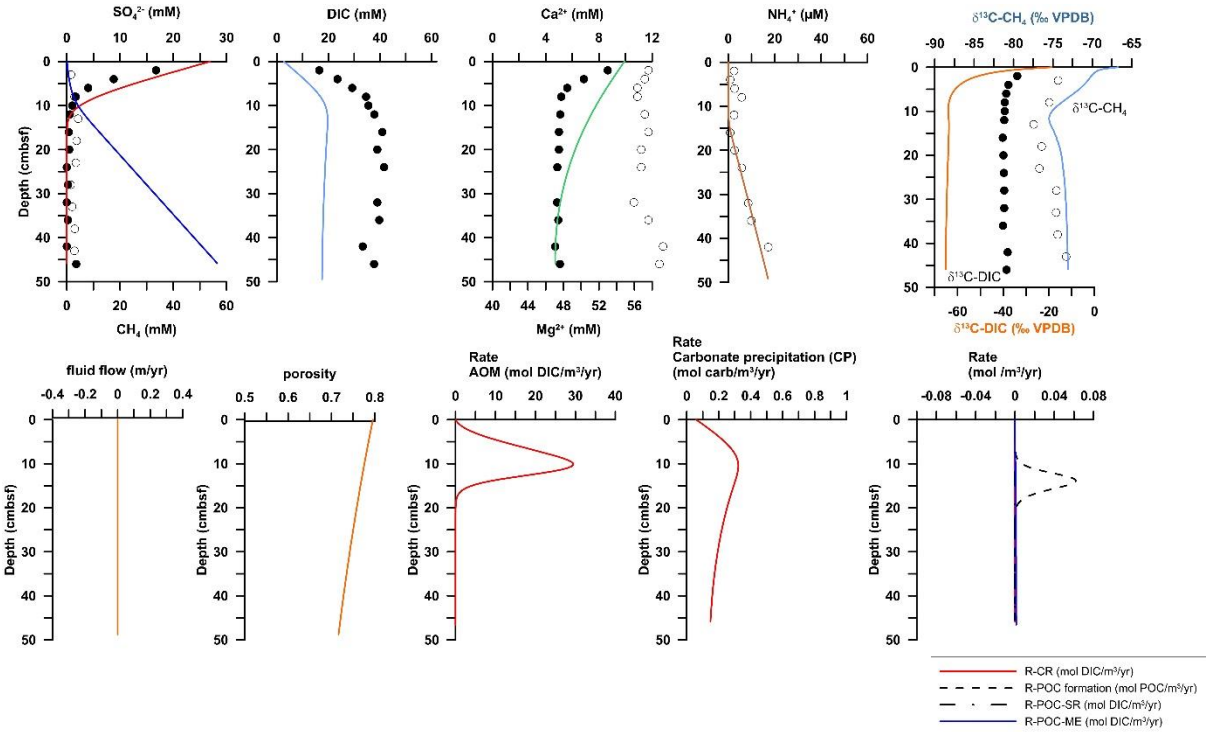

Figure S2: Model results for PC017 with no fluid flow and a no CO_2 reduction below the SMT. The black dots represent measured pore water data, the solid lines represent the best fit of our model. The upper right graph includes measured data for δ^{13}C-DIC (filled dots) and δ^{13}C-CH4 (circles). The lower right graph includes the depth profiles of the rates of CO_2 reduction (R-CR) organoclastic sulphate reduction (R-POC-SR) and organic matter degradation by fermentation (R-POC-ME). Rates of AOM, POC-SR, POC-ME and R-CR are all expressed in mol DIC/m^3/yr to make them easier to compare.

Table S2: Depth integrated rates of the different model runs

Run	R-AOM mole DIC/bulk m^2/yr	R-CR mole DIC/bulk m^2/yr	R-CP mole carb/bulk m^2/yr	R-POC-SR mole DIC/bulk m^2/yr	R-POC-ME mole DIC/bulk m^2/yr
MeBo Seep Site SW	0.236	0.000	0.025	0	0.006
PC017-no fluid advection	2.346	-0.217	0.113	0	0.001
PC017-no fluid advection +no CR	2.258	0	0.149	0	0.001
PC017 best fit (high fluid advection)	0.478	-0.068	0.059	0	0.001

3 Data tables

Table S3: Measured pore water concentrations

Core	Depth (cmbsf)	total alkalinity (mM)	Fe^{2+} (µM)	Mg^{2+} (mM)	Ca^{2+} (mM)	Na^{+} (mM)	Mn^{2+} (µM)	Sr^{2+} (µM)	SO_4^{2-} (mM)	δ^{13}C-DIC (‰VPDB)	PO_4^{3-} (µM)	NH_4^{+} (µM)
PC007	1	19.0	0.0	53.1	8.1	461.1	1.0	64.6	17.07	-30.5	3.9	6.5
PC007	5	30.8	0.0	53.5	6.4	469.8	0.1	47.6	10.05	-30.7	3.1	6.5
PC007	9	45.8	0.0	51.8	4.6	461.1	0.0	30.9	0.00	-31.7	4.8	2.5
PC007	13	50.1	0.0	51.4	4.3	469.8	0.0	28.0	0.00	-32.4	2.3	1.0
PC007	17	49.0	0.0	51.8	4.5	465.4	0.0	29.4	0.00	-33.1	2.5	2.4
PC007	21	48.3	0.0	50.6	4.8	461.1	0.0	34.5	0.60	-35.1	3.1	2.0
PC007	25	54.0	0.0	52.2	5.0	474.1	0.0	34.8	0.00	-35.4		
PC007	29	55.9	0.0	51.0	5.0	469.8	0.0	35.8	0.29	-34.5		
PC009	2	37.8	0.0	50.6	5.6	478.5	0.0	58.2	3.56	-25.1		
PC009	4	41.1	0.0	51.4	5.5	469.8	0.0	55.5	2.32	-25.9	1.0	1.0
PC009	6	49.6	0.0	50.2	5.0	469.8	0.0	52.3	1.63	-24.7	0.5	0.0
PC009	8	31.0		48.5	4.7	452.4	0.9	47.6	1.22		1.0	0.5
PC009	10	51.1	0.0	50.2	4.8	469.8	0.0	49.1	1.10	-25.8	1.0	1.0
PC009	12	47.8		49.0	4.5	456.7	0.0	46.1	0.42	-26.1	0.3	1.1
PC009	14	47.1	0.0	43.2	4.0	404.1	0.0	40.3	0.00	-26.9		
PC009	16	57.7	0.0	50.6	4.6	474.1	0.0	47.0	0.17	-27.1	0.6	8.5
PC009	18	50.5	0.0	50.2	4.5	469.8	0.0	46.1	0.16	-28.7	0.6	0.5
PC017	2	17.0	0.0	57.6	8.7	526.3	0.0	69.8	16.8	-33.9	3.7	2.5
PC017	4	26.3	0.0	57.2	6.9	530.7	0.0	51.0	8.8	-37.7	0.8	0.8
PC017	6	32.9	0.0	56.4	5.6	517.6	0.0	39.8	4.0	-38.7	6.3	2.7
PC017	8	38.9	0.0	56.4	5.2	530.7	0.0	35.0	1.7	-39.4	6.6	5.8
PC017	10	40.2	0.0						1.1	-39.3		
PC017	12	42.5	0.0	57.2	5.1	526.3	0.0	33.3	0.6	-39.6	3.7	2.5
PC017	16	45.6	0.0	57.6	5.0	535.0	0.8	33.2	0.4	-40.2	0.8	0.8
PC017	20	43.7	0.0	56.8	5.0	522.0	1.0	33.0	0.5	-40.0	6.3	2.7
PC017	24	46.0	0.0	56.8	4.9	522.0	1.3	32.4	0.0	-39.7	6.6	5.8
PC017	28		0.0						0.3	-39.5		
PC017	32	44.2	0.0	55.9	4.8	526.3	1.6	31.3	0.0	-39.5	3.4	8.6
PC017	36	44.9	0.0	57.6	4.9	539.4	1.8	31.7	0.2	-40.1	3.9	9.9
PC017	42	38.3	0.0	59.2	4.7	561.1	1.5	31.5	0.0	-38.1	3.9	17.2
PC017	46	42.5	0.0	58.8	5.1	556.8	2.1	33.8	1.8	-38.6		
PC020	3		1.2	49.0	10.0	448.0	5.9	88.5	28.5	-1.8	0.9	13.6
PC020	6		17.9	48.5	10.0	448.0	13.5	87.8	28.4	-2.7	2.8	10.8
PC020	8		20.0	49.4	10.0	452.4	14.2	87.7	28.1	-3.1	4.7	29.3
PC020	10	2.8	20.8	49.0	10.0	456.7	11.3	86.7	29.0	too low	6.7	13.3
PC020	12		14.4	50.6	10.6	478.5	9.4	94.6	29.6	-4.6	7.1	14.0
PC020	14		16.1	49.4	10.3	461.1	8.0	89.9	28.9	-5.1	8.1	14.8
PC020	16	2.6	13.2	49.8	10.1	461.1	7.6	88.2	28.7	-5.7	9.1	14.3
PC020	18		9.4	48.5	10.0	456.7	6.1	86.5	28.8	-6.3	7.1	14.1
PC020	20		2.8	46.9	9.5	448.0	5.9	84.1	29.1	-6.5	6.7	12.5
PC020	22		3.3	49.0	10.3	456.7	6.7	86.1	28.8	too low	7.1	10.9
PC020	26	3.2	1.4	50.6	10.5	461.1	6.6	87.4	28.7	-7.1	9.1	11.0
PC020	30		0.5	49.4	10.6	452.4	6.1	86.2	28.9	-7.5	6.2	10.5
PC020	34		0.2	48.5	10.4	456.7	6.1	85.0	29.4	-8.1	6.7	11.7
PC020	38		0.1	50.2	10.7	461.1	5.7	87.2	29.3	-8.1	6.7	8.6
PC020	42	3.3	0.0	49.4	10.6	452.4	7.0	85.6	28.8	-8.4	7.1	6.2
PC020	48		0.0	49.4	11.0	452.4	6.8	86.1	29.0	-8.8	6.2	10.7
PC020	54		0.0	49.4	10.9	452.4	6.5	85.6	29.0	-9.0	5.2	24.0
PC020	60	4.4	0.0	49.0	10.9	443.7	6.3	84.3	29.1	-9.3	3.3	10.8

PC021	-2	3.8	3.6	49.0	9.6	439.3	2.6	81.6	27.0	-12.8		
PC021	0	5.0	1.3	48.1	9.7	439.3	6.8	81.0	26.1	-16.2	1.4	11.5
PC021	2	6.2	0.3	48.1	9.2	439.3	9.5	78.7	24.6	-22.4	5.1	18.0
PC021	4	7.9	0.0	47.3	9.1	435.0	1.1	77.7	24.8	-23.7	2.4	15.2
PC021	6	14.5	0.0	46.1	7.7	432.4	0.0	68.0	19.0	-31.9	3.6	15.1
PC021	8	25.2	0.0	46.9	6.4	448.0	0.0	58.0	11.2	-36.3	3.1	4.2
PC021	10	26.5	0.0	46.1	5.6	435.0	0.0	51.8	7.6	-37.0	4.0	3.1
PC021	14	33.5	0.0	46.9	4.7	443.7	0.0	45.1	2.1	-37.4	4.3	3.2
PC021	18	25.0	0.0	46.9	5.1	435.0	0.0	47.7	6.1	-36.6	10.8	6.2
PC021	22	21.2	0.0	48.1	6.8	439.3	0.4	60.7	15.4	-33.2	1.8	6.2
PC021	26	22.5	0.0	48.5	6.4	443.7	0.5	57.5	12.9	-34.4	8.5	7.0
PC021	30	34.1		46.1	4.6	439.3	0.5	44.3	1.6	-37.6	7.3	20.3

Table S4:Methane concentration, carbon and hydrogen isotopes of methane ($\delta^{13}C$-CH_4, $\delta^{2}H$-CH_4), and carbon isotopes of ethane ($\delta^{13}C$-C_2H_6)

	Depth (cmbsf)	CH_4 mM	CH_4 $\delta^{13}C$ (‰VPDB)	CH_4 $\delta^{2}H$ (‰SMOW)	C_2H_6 $\delta^{13}C$ (‰VPDB)
PC009	5	4.08	-66.6	-165	-28.2
	11	5.90	-69.0	-170	-28.7
	15	11.87	-67.0	-171	-26.6
	19	5.27	-65.8	-163	-27.3
PC017	3	1.64	-74.3	-175	-25.2
	8	2.99	-75.4	-172	-25.2
	13	4.31	-77.4	-176	-25.2
	18	3.69	-76.4	-170	-25.7
	23	3.45	-76.7	-177	-25.2
	28	1.50	-74.6	-180	-26.3
	33	2.07	-74.6	-178	-25.8
	38	3.00	-74.4	-177	-25.7
	43	2.92	-73.3	-175	-26
PC021	3	0.30	-61.6	-165	-27
	8	0.30	-64.4	-189	-26.7
	13	0.76	-62.5	-169	-26.1
	18	1.49	-62.7	-179	-25.3
	23	2.79	-72.8	-178	-27.4
	28	1.79	-74.3	-172	-27.3
PC020	8	0.004	-51.7		
	13	0.003	-51.4		
	18	0.003	-54.9		
	23	0.003	-51.9		
	28	0.005	-53.9		
	33	0.003	-53.5		
	38	0.003	-56.4		
	43	0.004	-57.0		
	48	0.009	-54.5		
	53	0.009	-53.5		
	58	0.004	-54.3		
	63	0.009	-53.8		

Table S5: total carbon (TC), total organic carbon (TOC), δ^{13}C-TOC, and total nitrogen (TN) content

	Depth cmbsf	TC wt%	TOC wt%	δ^{13}C-TOC V-PDB (‰)	TN wt%
PC007	1	2.9	1.8	-28.1	0.3
	3	2.6	1.7	-28.0	0.3
	6	2.8	1.9	-26.5	0.3
	8	2.5	1.8	-27.1	0.3
	11	2.6	1.9	-26.3	0.3
	13	2.9	1.9	-27.3	0.3
	15	2.5	1.8	-26.9	0.2
	17	2.4	1.9	-26.9	0.2
	20	2.5	1.9	-26.9	0.3
	22	2.4	1.8	-27.4	0.3
	24	2.3	1.7	-27.4	0.3
	27	2.3	1.6	-28.0	0.2
	29	2.0	1.6	-29.1	0.2
	31	2.3	1.6	-29.4	0.2
	34	2.4	1.7	-28.8	0.2
	36	2.4	1.7	-30.7	0.2
PC009	1	2.6	1.9	-27.6	0.3
	3	2.6	1.8	-28.2	0.3
	6	2.7	1.6	-28.1	0.2
	8	3.0	1.8	-29.1	0.2
	10	3.5	1.5	-29.8	0.2
	13	3.5	1.5	-30.4	0.2
	15	3.9	1.5	-31.1	0.2
	17	4.2	1.4	-30.8	0.2
	19	5.0	1.3	-31.2	0.2
	22	5.6	1.3	-33.1	0.2
	25	6.1	1.3	-34.5	0.2
PC017	4	2.9	2.0	-24.5	0.3
	6	2.8	1.9	-24.2	0.2
	8	2.7	1.8	-24.5	0.2
	11	2.3	1.9	-23.9	0.2
	14	2.3	2.0	-24.4	0.3
	16	2.2	2.0	-24.4	0.3
	19	2.2	2.0	-24.0	0.3
	21	2.1	1.9	-23.7	0.3
	24	2.1	1.8	-23.8	0.2
	26	2.0	1.7	-23.9	0.2
	28	2.1	1.8	-23.6	0.2
	31	2.1	1.8	-23.9	0.2
	33	2.1	1.8	-24.6	0.2
	35	2.1	1.7	-25.8	0.2
	38	2.1	1.7	-25.7	0.2
	40	2.1	1.7	-26.0	0.2
	42	2.2	1.8	-27.2	0.2
	44	2.2	1.7	-27.4	0.2
	47	2.3	1.6	-27.2	0.2
	49	2.1	1.6	-28.9	0.2

	52	2.1	1.6	-30.2	0.2
PC020	1	2.9	1.5	-23.2	0.2
	3	3.0	1.6	-23.1	0.2
	6	2.9	1.4	-23.1	0.2
	8	2.9	1.4	-23.1	0.2
	10	2.6	1.3	-23.1	0.2
	13	2.6	1.3	-23.1	0.2
	15	2.6	1.3	-23.1	0.2
	17	2.4	1.4	-23.1	0.2
	20	2.2	1.4	-23.2	0.2
	22	2.1	1.4	-23.3	0.2
	24	1.9	1.3	-23.4	0.2
	27	1.9	1.3	-23.5	0.2
	29	1.8	1.3	-23.5	0.2
	31	1.7	1.3	-23.7	0.2
	34	1.6	1.3	-23.6	0.2
	36	1.5	1.1	-24.0	0.1
	38	1.3	1.0	-24.2	0.1
	41	1.6	1.2	-24.3	0.2
	43	1.8	1.3	-24.3	0.2
	46	1.9	1.3	-24.2	0.2
	48	2.0	1.3	-24.1	0.2
	50	2.1	1.3	-24.0	0.2
	53	2.0	1.2	-24.0	0.2
	55	1.9	1.2	-23.9	0.2
	57	2.1	1.3	-24.2	0.1
	60	2.1	1.3	-24.3	0.2
	63	2.1	1.3	-24.3	0.2
	65	2.2	1.3	-24.0	0.2
	68	2.2	1.3	-23.9	0.2
	71	2.1	1.3	-24.0	0.2
PC021	3	2.7	1.8	-25.2	0.3
	5	2.6	1.4	-24.3	0.2
	8	2.7	1.4	-23.9	0.2
	11	2.7	1.4	-23.8	0.2
	14	2.6	1.3	-23.4	0.2
	19	2.6	1.5	-23.7	0.2
	22	2.5	1.5	-24.2	0.2
	25	2.2	1.6	-24.2	0.2
	27	2.0	1.7	-25.1	0.2
	29	2.0	1.5	-25.9	0.2
	32	1.9	1.5	-26.6	0.2
	34	1.9	1.5	-27.7	0.2
	36	2.1	1.4	-29.2	0.2
	38	2.1	1.4	-30.7	0.2

Magnetic susceptibility and XRF scan Ca/Ti in extra excel table

References

Boudreau, B., 1997. Diagenetic models and their implementation: modelling transport and reactions in aquatic sediments. Springer, Berlin, Heidelberg, NY, 414 pp

Hong, W.-L., Torres, M., Kim, J.-H., Choi, J., Bahk, J.-J., 2013. Carbon cycling within the sulfate-methane-transition-zone in marine sediments from the Ulleung Basin. Biogeochemistry, 115(1-3): 129-148.https://doi.org/10.1007/s10533-012-9824-y

Hong, W.-L., Torres, M.E., Kim, J.-H., Choi, J., Bahk, J.-J., 2014. Towards quantifying the reaction network around the sulfate–methane-transition-zone in the Ulleung Basin, East Sea, with a kinetic modeling approach. Geochimica et Cosmochimica Acta, 140: 127-141.http://dx.doi.org/10.1016/j.gca.2014.05.032

Nauhaus, K., Albrecht, M., Elvert, M., Boetius, A., Widdel, F., 2007. In vitro cell growth of marine archaeal-bacterial consortia during anaerobic oxidation of methane with sulfate. Environmental Microbiology, 9(1): 187-196.https://doi.org/10.1111/j.1462-2920.2006.01127.x

Nauhaus, K., Boetius, A., Krüger, M., Widdel, F., 2002. In vitro demonstration of anaerobic oxidation of methane coupled to sulphate reduction in sediment from a marine gas hydrate area. Environmental Microbiology, 4(5): 296-305.https://doi.org/10.1046/j.1462-2920.2002.00299.x

Pohlman, J.W., Kaneko, M., Heuer, V.B., Coffin, R.B., Whiticar, M., 2009. Methane sources and production in the northern Cascadia margin gas hydrate system. Earth and Planetary Science Letters, 287(3–4): 504-512.http://dx.doi.org/10.1016/j.epsl.2009.08.037

Rees, C.E., 1973. A steady-state model for sulphur isotope fractionation in bacterial reduction processes. Geochimica et Cosmochimica Acta, 37(5): 1141-1162.https://doi.org/10.1016/0016-7037(73)90052-5

Steefel, C.I., Appelo, C.A.J., Arora, B., Jacques, D., Kalbacher, T., Kolditz, O., Lagneau, V., Lichtner, P.C., Mayer, K.U., Meeussen, J.C.L., Molins, S., Moulton, D., Shao, H., Šimůnek, J., Spycher, N., Yabusaki, S.B., Yeh, G.T., 2015. Reactive transport codes for subsurface environmental simulation. Computational Geosciences, 19(3): 445-478.https://doi.org/10.1007/s10596-014-9443-x

Vavilin, V., 2013. Estimating changes of isotopic fractionation based on chemical kinetics and microbial dynamics during anaerobic methane oxidation: apparent zero-and first-order kinetics at high and low initial methane concentrations. Antonie van Leeuwenhoek, 103(2): 375-383.https://doi.org/10.1007/s10482-012-9818-8

Whiticar, M.J., 1999. Carbon and hydrogen isotope systematics of bacterial formation and oxidation of methane. Chemical Geology, 161(1–3): 291-314.http://dx.doi.org/10.1016/S0009-2541(99)00092-3

Yoshinaga, M.Y., Holler, T., Goldhammer, T., Wegener, G., Pohlman, J.W., Brunner, B., Kuypers, M.M.M., Hinrichs, K.-U., Elvert, M., 2014. Carbon isotope equilibration during sulphate-limited anaerobic oxidation of methane. Nature Geoscience, 7(3): 190-194.https://doi.org/10.1038/ngeo2069

Zeebe, R.E., Wolf-Gladrow, D., 2001. CO2 in Seawater: Equilibrium, Kinetics, Isotopes, 65. Elsevier Science, 360 pp